Current Research in Neurobiology 4 (2023) 100090

Contents lists available at ScienceDirect

Current Research in Neurobiology

journal homepage: www.sciencedirect.com/journal/current-research-in-neurobiology

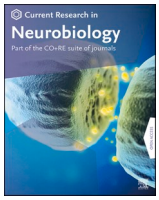

Alterations of fractional anisotropy throughout cortico-basal ganglia gray matter in a macaque model of Huntington's Disease

Alison R. Weiss [a,*], William A. Liguore [a], Kristin Brandon [a], Xiaojie Wang [a,b], Zheng Liu [a,b], Christopher D. Kroenke [a,b,c], Jodi L. McBride [a,c]

[a] Division of Neuroscience, Oregon National Primate Research Center, Beaverton, OR, USA, 97006
[b] Advanced Imaging Research Center, Oregon Health and Science University, Portland, OR, USA, 97239
[c] Department of Behavioral Neuroscience, Oregon Health and Science University, Portland, OR, USA, 97239

ARTICLE INFO

Keywords:
Diffusion tensor imaging
Fractional anisotropy
Cortico-basal ganglia
Adeno-associated virus
Huntington's disease

ABSTRACT

We recently generated a nonhuman primate (NHP) model of the neurodegenerative disorder Huntington's disease (HD) using adeno-associated viral vectors to express a fragment of mutant HTT protein (mHTT) throughout the cortico-basal ganglia circuit. Previous work by our group established that mHTT-treated NHPs exhibit progressive motor and cognitive phenotypes which are accompanied by mild volumetric reductions of cortical-basal ganglia structures and reduced fractional anisotropy (FA) in the white matter fiber pathways interconnecting these regions, mirroring findings observed in early-stage HD patients. Given the mild structural atrophy observed in cortical and sub-cortical gray matter regions characterized in this model using tensor-based morphometry, the current study sought to query potential microstructural alterations in the same gray matter regions using diffusion tensor imaging (DTI), to define early biomarkers of neurodegenerative processes in this model. Here, we report that mHTT-treated NHPs exhibit significant microstructural changes in several cortical and subcortical brain regions that comprise the cortico-basal ganglia circuit; with increased FA in the putamen and globus pallidus and decreased FA in the caudate nucleus and several cortical regions. DTI measures also correlated with motor and cognitive deficits such that animals with increased basal ganglia FA, and decreased cortical FA, had more severe motor and cognitive impairment. These data highlight the functional implications of microstructural changes in the cortico-basal ganglia circuit in early-stage HD.

1. Introduction

Huntington's disease (HD) is a neurodegenerative disorder characterized by progressive motor disfunction (typically involving hyperkinetic involuntary movements known as chorea), cognitive impairment, and mood disturbances. HD is caused by an expanded CAG repeat in exon 1 of the *HTT* gene on chromosome 4 (Huntington's Disease Collaborative Research Group, 1993), CAG repeats above 40 confer a toxic-gain-of-function to the mHTT protein which misfolds, forms into cellular aggregates, induces gliosis and leads to neuronal death (Zuccato et al., 2010). In patients, HD neuropathology is most severe in the caudate and putamen, but many other cortical and sub-cortical regions with striatal afferents are also impacted including the prefrontal cortex, anterior cingulate cortex, motor cortex, globus pallidus, thalamus, and amygdala, among others (Glass et al., 1993, 2000; Rosas et al., 2008; Allen et al., 2009; Majid et al., 2011).

To recapitulate this pattern of widespread circuit disfunction in a macaque model of HD, we injected adult animals in the caudate and putamen with a 1:1 combination of adeno associated virus serotype 2 (AAV2) and AAV2.retro, an AAV2 capsid mutant with potent retrograde transport capability (Tervo et al., 2016). Both vectors expressed a pathogenic fragment of human mutant *HTT* with 85 CAG repeats (HTT85Q). Biodistribution studies indicated that animals develop hallmark mHTT-positive aggregates throughout the cortico-basal ganglia network as early as 10 weeks post-AAV delivery (Weiss et al., 2020). Longer-term longitudinal studies in this model indicate that HTT85Q treated macaques exhibit behavioral and neuropathological dysfunction over the course of 30 months that are similar to those observed in HD patients, including hallmark behavioral manifestations associated with cortico-striatal dysfunction (e.g. chorea, cognitive impairment, etc.), mild volumetric reductions of cortico-basal ganglia structures, and reduced fractional anisotropy (FA) in the white matter fiber pathways

* Corresponding author. Division of Neuroscience, Oregon National Primate Research Center, 505 NW 185th Avenue, Beaverton, OR, 97006, USA.
E-mail address: weissa@ohsu.edu (A.R. Weiss).

https://doi.org/10.1016/j.crneur.2023.100090
Received 6 November 2022; Received in revised form 14 April 2023; Accepted 16 May 2023
Available online 30 May 2023

interconnecting those cortical and subcortical gray matter brain regions (Weiss et al., 2022). This pattern of distributed neuropathology, coupled with the mild but clinically relevant behavioral features, closely mirrors findings observed in early-stage human HD patients, and highlights the critical involvement of cortico-basal ganglia circuitry in HD.

Diffusion imaging can be used to generate MRI-based maps of the random translational motion of water molecules in the brain, which is hindered by cell membranes and fibers. Using this technique, microstructural properties of brain tissue can be inferred. Although diffusion tensor imaging (DTI) is often used to quantify microstructural pathological changes in white matter, it is also possible to investigate changes in tissue integrity in gray matter brain regions using this imaging technique. Studies of pre-symptomatic HD gene carriers and early-stage patients suggest that DTI may be able to capture some of the earliest features of HD-pathology in gray matter, occurring before robust cell loss and regional atrophy. A clear and consistent pattern of increased FA in the putamen and globus pallidus has been described in pre-manifest/early symptomatic HD patients; followed by decreasing FA in gray matter areas including the ventromedial frontal cortex, insula cortex, and the cerebellum in more advanced HD patients (Rosas et al., 2006; Douaud et al., 2009; Sritharan et al., 2010; Delmaire et al., 2013; Georgiou-Karistianis et al., 2013; Sanchez-Castaneda et al., 2013; Sprengelmeyer et al., 2014; Estevez-Fraga et al., 2020).

Some animal models of HD in other species show increased subcortical FA during early stages of disease progression, including sheep (O'Connell et al., 2020), rats (Antonsen et al., 2013), and mice (Petrella et al., 2018; Simmons et al., 2021), which has been associated with increased gliosis and reductions in striatal matrix fibers assessed by immunohistochemical evaluations; for review see (Gatto and Weissmann, 2019). In one study using the R6/2 mouse model, striatal FA levels were preserved following treatment with small molecules designed to promote trophic signals, demonstrating the suitability of this measure as an imaging biomarker for therapeutic efficacy (Simmons et al., 2021). However, few animal studies have reported areas of decreased FA in cortical areas akin to those observed in more advanced HD patient populations.

HTT85Q-treated macaques exhibit mild regional atrophy in cortico-basal ganglia structures, suggesting that there is not robust neuronal loss in this model, out to 30-months. Yet, the same HTT85Q-treated macaques exhibit motor and cognitive phenotypes known to be associated with impaired cortico-basal ganglia function, suggesting that there may be microstructural alterations driving these behavioral phenotypes. In the current study, we sought to characterize potential changes in gray matter FA (both increases and decreases) in the HTT85Q model of HD, for the purpose of validating this clinical imaging finding in a relevant large animal model of this disorder, as well as identifying an early imaging biomarker of disease progression that can be used as an outcome measure in future therapeutic assessments.

2. Materials & methods

2.1. Animals

This study involved 17 adult *Rhesus Macaques (Macaca mulatta)* (age 6–13), (n = 12 female, n = 5 male) that received MRI-guided stereotaxic injections of a 1:1 mixture of recombinant adeno-associated viral vectors, serotypes AAV2 and AAV2.retro, each expressing a fragment of human mutant *HTT* (*mHTT)* with 85 CAG repeats (group HTT85Q, n = 6), a control fragment of human HTT bearing 10 CAG repeats (group HTT10Q, n = 6), or buffer (n = 5), into the caudate and putamen. Details of the surgical procedures and animal preparations have been previously reported (Weiss et al., 2022). One animal in the HTT85Q group was unavailable for assessment at the 30m timepoint.

Monkeys were pair housed on a 12-h light/dark cycle, provided with monkey chow rations twice daily, produce and enrichment once daily, and given ad libitum access to water. Animal health and well-being checks were conducted by Oregon National Primate Research Center (ONPRC) veterinary and technical staff daily. The Institutional Animal Care and Use Committee and the Institutional Biosafety Committee at the ONPRC and Oregon Health and Science University approved all experimental procedures, and all of the guidelines specified in the National Institutes of Health Guide for the Care and Use of Laboratory Animals (2011) were strictly followed.

2.2. Scan acquisition

Diffusion tensor imaging (DTI) data were collected at 3-, 6-, 9-, 14-, 20-, and 30-month timepoints post AAV-delivery using a Siemens Prisma whole body 3T MRI system (Erlangen, Germany) with a 16-channel pediatric head rf coil, using the same acquisition sequences that were developed for the ONPRC18 multimodal brain atlas (Weiss et al., 2021). In brief, animals were anesthetized with Ketamine HCl (15 mg/kg IM) and maintained via inhalation of 1–2% isoflurane gas vaporized in 100% oxygen for the scan duration to prevent motion artifacts and to ensure their safety. The diffusion-weighted (DW) imaging employed a spin-echo planar imaging (EPI) sequence with 1.0 mm isotropic voxels and TR/TE = 6700 ms/73 ms, GRAPPA factor = 2, and echo train length = 52. We collected 7 repetitions of n = 6 b0 volumes and n = 30 DW volumes with b = 1000 s/mm^2 (anterior-posterior phase-encoding direction), as well as a single b0 volume with a reversed (posterior-to-anterior) phase-encoding direction to correct for susceptibility-induced distortions.

DW volumes were subsequently unwarped, de-noised, and eddy corrected using approaches identical to those reported previously, (Weiss et al., 2021), and the DTI-TK toolkit was used to fit the corrected volume to a single tensor (DTI) model. This procedure was completed for data collected from each animal at each timepoint separately. Next, individual DTI tensor maps were aligned to the ONPRC18 tensor template with b-spline non-linear registrations (implemented with DTI-TK), and parameter maps generated in a co-aligned template space for subsequent voxel wise analyses.

2.3. Image data analysis

DTI parameter maps were compared across timepoints for each group separately using the FSL Sandwich Estimator (FSL-SwE) tool (Guillaume et al., 2014) using identical analysis parameters that were applied to earlier studies of structural MRI and white matter DTI in the same animals (Weiss et al., 2022). This included threshold free cluster enhancement (TFCE) with 500 permutations only (Winkler et al., 2014). Family-wise error correction was not employed, however, an increased threshold of $p < 0.01$ was applied to all of the results. Additionally, to focus the investigation on microstructural changes in cortical and subcortical areas only, a gray matter mask derived from the ONPRC18 labelmap (Weiss et al., 2021) was used to restrict the voxelwise comparisons to cortical and subcortical gray matter regions (excluding white matter).

To visualize the results, 'lightbox' style images were created using FSLeyes (v6.0.2) with $p < 0.01$ thresholded p-value maps for each contrast overlaying the ONPRC18 FA template. Next, to enable assignment to specific anatomical regions, we calculated the percent area of each region of interest (ROI) defined by the ONPRC18 labelmap exhibiting $p < 0.01$ voxels using FSL tools to threshold and binarize and the p-value maps, and then AFNI tools (3dcalc) to extract volume information. The percent volumes of each ROI with significant ($p < 0.01$) changes from baseline were then plotted for each timepoint in a histogram. To assess the magnitude of these changes, 'difference' maps were calculated by subtracting baseline from each subsequent timepoint (implemented using fslmaths commands). Then, two different masks created from the 30-month thresholded p-value maps (one for areas of FA increases, one for areas of FA decreases) were used to determine the changes in diffusion parameters from baseline under these areas at each

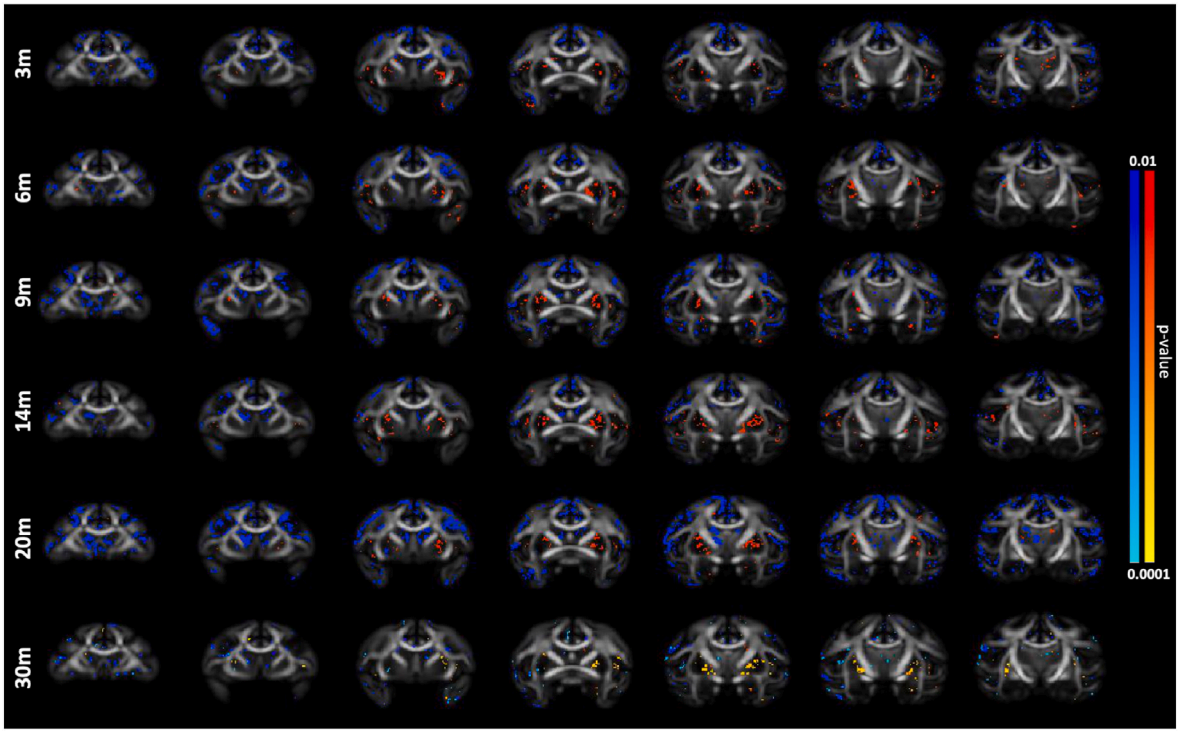

Fig. 1. Altered fractional anisotropy (FA) in gray matter brain regions of HTT85Q-treated macaques. Voxel wise comparisons in HTT85Q animals between baseline and each experimental timepoint (shown separately on each row) overlaid onto the ONPRC18 FA template (Weiss et al., 2021). Cool (blue/turquoise) voxels represent significant ($p < 0.01$) FA reductions, warm (red/yellow) voxels represent significant ($p < 0.01$) FA increases. No significant ($p < 0.01$) changes in either direction was observed in the control groups (HTT10Q, Buffer; not pictured). (For interpretation of the references to colour in this figure legend, the reader is referred to the Web version of this article.)

timepoint (3m–30m). This calculation was made together for all gray matter areas, rather than for each ROI separately, and subsequently assessed with two-way mixed effects ANOVAs that included contrasts for the Group*Time interaction and post-hoc group comparisons at each timepoint using the Tukey correction for multiple comparisons, as well as within-group comparisons across timepoints. Analysis of other diffusion metrics (Medial Diffusivity, MD; Radial Diffusivity, RD; Axial Diffusivity, AD) was conducted in a similar manner. Supplementary Figure 1 provides a schematic overview of this analysis workflow.

2.4. Imaging and behavioral correlations

Motor and cognitive phenotypes of the animals assessed in the current study have been reported elsewhere (Weiss et al., 2022), and were used for the correlational analyses reported here. Detailed descriptions of the behavioral methods were previously published (Weiss et al., 2022). Briefly, motor phenotypes were assessed using a nonhuman primate neurological rating scale (modeled after the Unified Huntington's Disease Rating Scale) in which higher scores are associated with

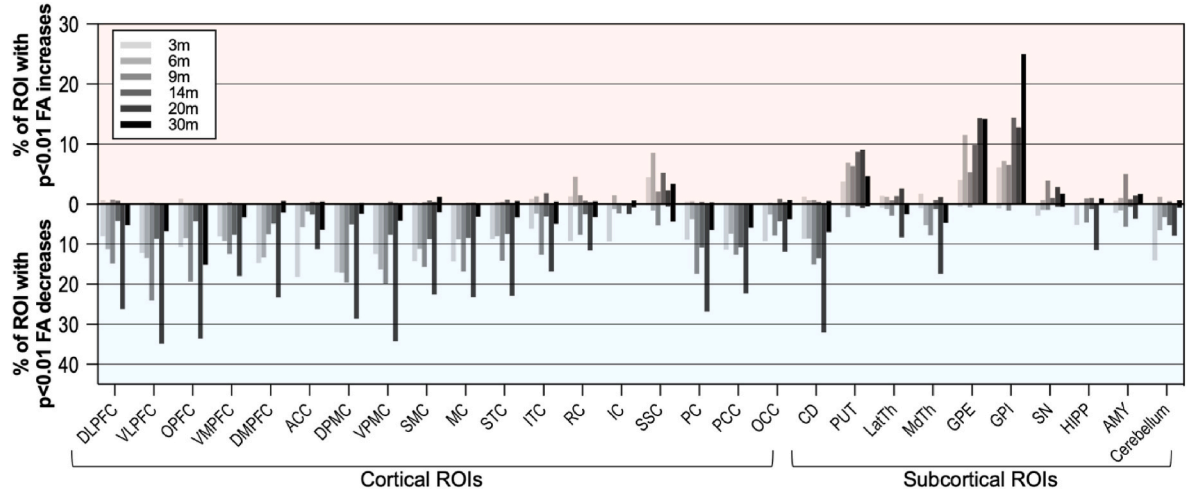

Fig. 2. Regional quantification of FA changes in gray matter brain regions of HTT85Q-treated animals. The volume of each ROI showing significant FA changes illustrated in Fig. 1 were quantified using the gray matter labelmap from the ONPRC18 atlas (Weiss et al., 2021). Data are plotted in a histogram, with bars shaded according to timepoint. The top panel (red background) represents the areas with significant FA increases (corresponding to warm voxels in Fig. 1), and the bottom panel (blue background) represents the areas with significant FA decreases (corresponding to cool voxels in Fig. 1). (For interpretation of the references to colour in this figure legend, the reader is referred to the Web version of this article.)

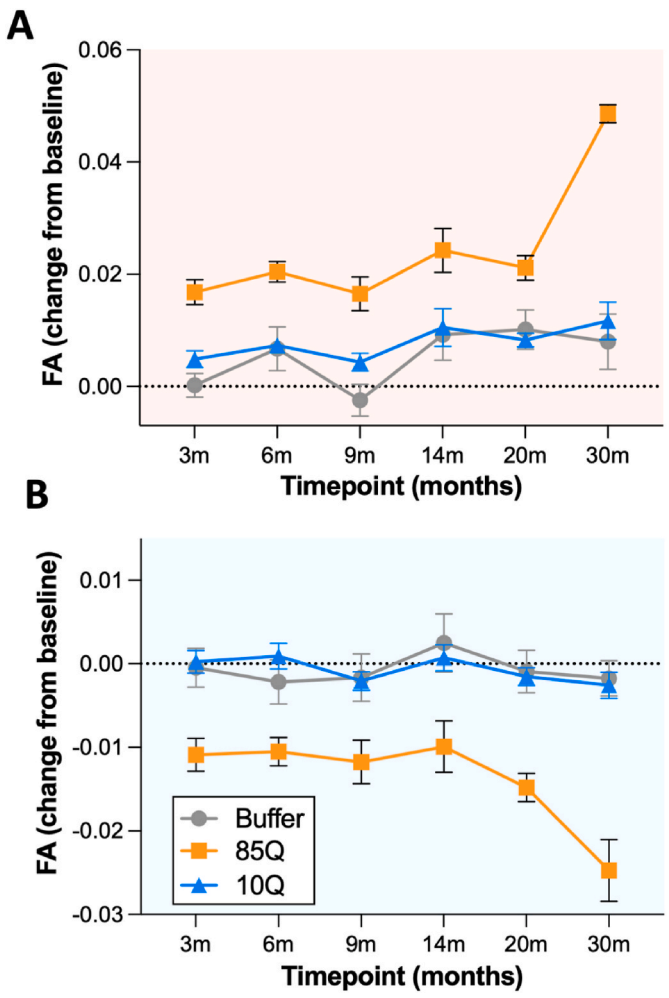

Fig. 3. HTT85Q-treated macaques show progressive alterations in FA compared to controls. Masks created from the 30-month thresholded p-value maps (shown in Fig. 1) were used to determine the magnitude of changes in FA at each timepoint. Data were analyzed with two-way mixed effects ANOVAs that included post-hoc between group comparisons at each timepoint and within group comparisons across timepoints. Panel **(A)** illustrates areas with significant FA increases, and panel **(B)** areas with significant FA decreases. HTT85Q-treated animals differed significantly ($p < 0.05$) from both Buffer and HTT10Q control groups at all the timepoints, whereas the control groups did not differ from each other (all $p > 0.05$). Additionally, for group HTT85Q only, the 30m timepoint differed significantly from all other timepoints in areas of FA increases (**A**) and decreases (**B**). Supplementary Tables 1–4 provide detailed statistical parameters for these comparisons.

more severe motor phenotypes (Huntington Study Group, 1996; McBride et al., 2011). Fine motor skills were assessed using a Lifesaver Retrieval Task (Chan et al., 2015) in which longer retrieval latencies are associated with impaired fine motor performance. Cognitive impairment was assessed using the 3-Choice Spatial Delayed Response (SDR) task in which lower scores are associated with impairment of spatial working memory processes (Bachevalier and Mishkin, 1986). Motor scores were available from all 17 animals, and 15 of 17 animals completed the cognitive assays. To investigate correspondence between the diffusion changes in gray matter areas and behavioral manifestations, the behavioral and imaging measures were first collapsed across time (averaged), and then correlated using 2-tailed Pearson tests.

3. Results

3.1. Altered diffusion in cortex and basal ganglia

Comparisons between baseline and subsequent timepoints revealed that HTT85Q-treated animals had numerous areas of gray matter with significant ($p < 0.01$) FA changes over the course of the 30-month study. In contrast, significant changes were not seen in either control group ($p < 0.01$). Fig. 1 shows p-value maps illustrating areas of significant FA increases and decreases at each timepoint for HTT85Q-treated animals, and Supplementary Figures 2-4 show p-value maps from the other diffusion metrics (MD, RD, AD). By 3-months post-surgery, HTT85Q-injected animals showed areas in the head of the caudate, as well regions of prefrontal, motor, temporal, and parietal cortex with significant reductions in FA; and areas of the putamen and globus pallidus with significant increases in FA. These patterns persisted throughout the 30-month study duration, becoming more pronounced and focal between 20 and 30 months (smaller p-values). Examination of other diffusion metrics revealed that areas with reduced FA tended to also exhibit increased MD, RD, and AD; whereas areas with increased FA tended to exhibit reduced MD, RD, and AD (Supplementary Figures 2-4).

To further characterize the brain-wide pattern of the significant FA increases and decreases in group HTT85Q, the volume of the $p < 0.01$ areas was quantified using parcellations available in the ONPRC18 atlas for 28 bilateral gray matter brain regions, illustrated in Fig. 2. The analysis revealed a region-specific pattern, with areas comprising cortico-basal ganglia circuitry showing the most robust changes in FA. These brain regions also showed the most robust mHTT aggregate formation in this model, characterized by 2B4 (Weiss et al., 2020) and EM48 (Weiss et al., 2022) immunohistochemistry. There was also a clear pattern associated with the direction of FA changes: numerous cortical brain regions showed reduced FA, while most of the regions showing increased FA were in subcortical areas. Of note was the divergent pattern of significant changes in the striatum/basal ganglia, with regions of the caudate and thalamus showing significant FA decreases, and regions of the putamen and globus pallidus showing significant FA increases, compared to baseline. To quantify the magnitude of the FA changes in these brain regions, masks were created separately for regions of FA increase, and regions of FA decrease, using p-value maps from the final timepoint (30-months). The change in FA (from baseline) under these two masks was then calculated for each animal at each post-surgical timepoint and plotted separately (Fig. 3).

In gray matter regions with significantly increased FA (Fig. 3A), there was a significant Group*Timepoint interaction ($F(10,69) = 6.364$, $p < 0.0001$), as well as significant main effects of Group ($F(2,14) = 28.64$, $p < 0.0001$), and Timepoint ($F(5,69) = 19.80$, $p < 0.0001$). Post-hoc tests between groups at each timepoint revealed that HTT85Q-treated animals had significantly greater elevations in compared to both Buffer and HTT10Q groups at all timepoints measured (all $p < 0.05$). The HTT10Q control group did not differ significantly at any of the timepoints (all $p > 0.05$), but the Buffer group differed between the 3m and 20m timepoint, as well as between the 9m and 14m, 20m, and 30m timepoints (all $p < 0.05$). Additionally, HTT85Q treated animals showed FA changes at the 30m timepoint that differed significantly from all other timepoints, showing the progressive nature of this finding. Supplementary Tables 1 and 2 reports statistical parameters for these comparisons.

Similarly, in gray matter regions with significantly reduced FA (Fig. 3B), there was a Group*Timepoint interaction ($F(10,69) = 6.323$, $p,<0.0001$) as well as significant main effects of Group ($F(2,14) = 16.48$, $p = 0.0002$), and Timepoint ($F(5,69) = 14.28$, $p < 0.0001$). Post-hoc tests between groups at each timepoint demonstrated that HTT85Q-treated animals had significant reductions in FA compared to both Buffer and HTT10Q groups at all timepoints measured (all $p < 0.05$), whereas the Buffer and HTT10Q control groups did not differ significantly at any of the timepoints. Similar to the elevations in FA,

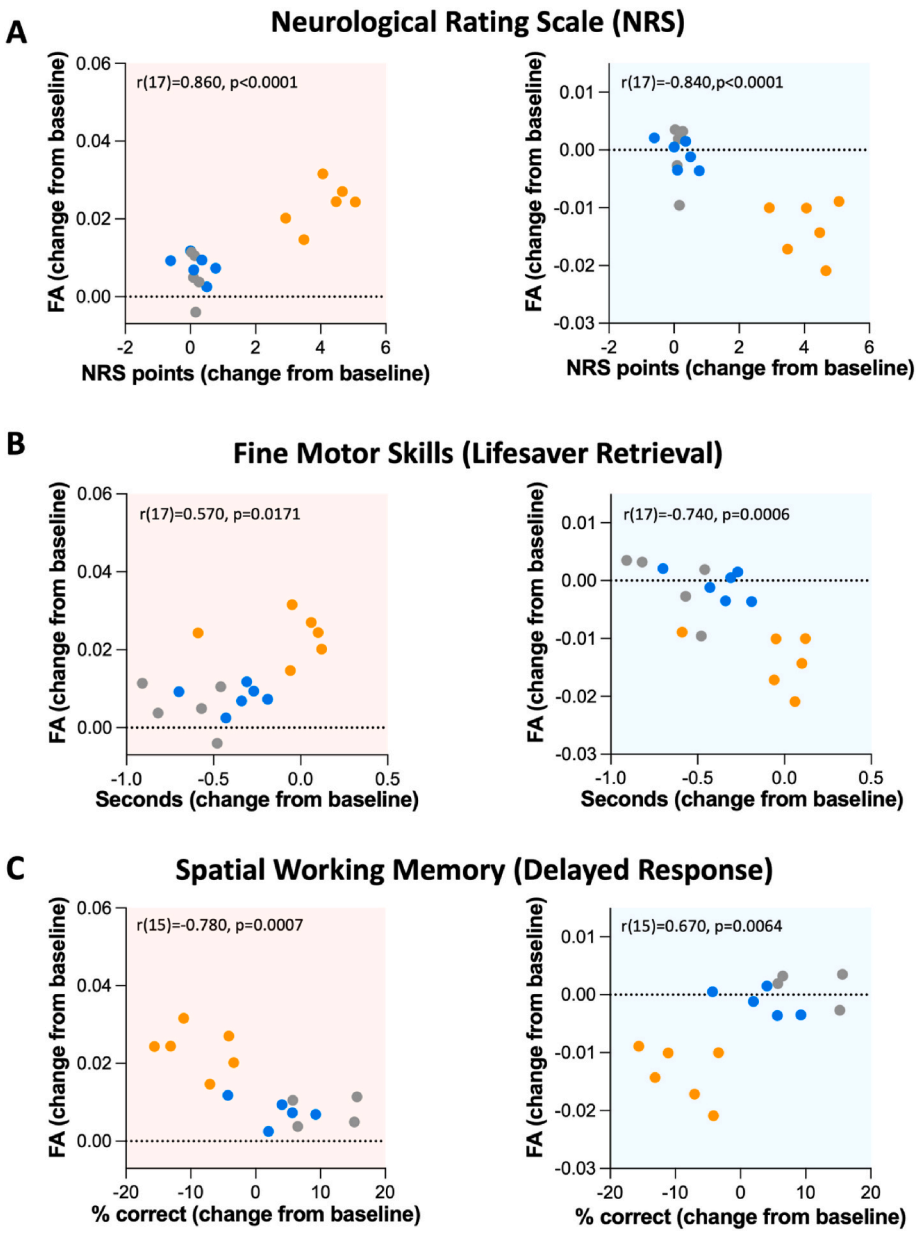

Fig. 4. Correspondence between FA alterations and behavioral scores. Increases in FA were significantly correlated with higher scores on the NHP Neurological Rating Scale (NRS) **(4A, left),** longer retrieval latencies in the Lifesaver task of fine motor skills (**4B, left**), and lower percentage correct on the 3-Choice SDR task of working memory (**4C, left**). Decreases in FA were significantly associated with higher NRS scores **(4A, right)**, longer Lifesaver retrieval latencies **(4B, right)** and lower percentage correct on the 3-Choice SDR task **(4C, right).** Data are collapsed across all timepoints. For NRS and Lifesaver, n = 17; for SDR, n = 15.

reductions in FA in HTT85Q-treated monkeys were also progressive in nature, with differences noted between the 30m timepoint and all other timepoints, as well as differences between the 14m and 20m timepoints ($p < 0.05$ for each). Supplementary Tables 3 and 4 report statistical parameters for each of the comparisons.

3.2. *Correspondence with behavioral impairments*

Behavioral measures of motor and cognitive function were collected from these animals shortly before each imaging session (Weiss et al., 2022). To probe the relationship between the observed DTI changes and behavioral phenotypes, two-tailed Pearson correlations were computed between FA and behavioral change scores, collapsed across the post-surgical timepoints. FA changes in gray matter were correlated with all three behavioral measures, such that greater increases in FA were significantly associated with motor deficits: higher scores on the NHP Neurological Rating Scale (NRS) ($r(17) = 0.860$, $p < 0.0001$), (Fig. 4A, left), longer retrieval latencies in the Lifesaver task of fine motor skills ($r(17) = 0.570$, $p = 0.0171$) (Fig. 4B, left); and cognitive impairment: lower percentage correct on the 3-Choice SDR task of working memory ($r(15) = -0.780$, $p = 0.0007$) (Fig. 4C, left). Additionally, greater decreases in FA were also significantly associated with worse motor and cognitive performance: higher NRS scores ($r(17) = -0.840$, $p < 0.0001$) (Fig. 4A, right), longer Lifesaver retrieval latencies ($r(17) = -0.740$, $p = 0.0006$) (Fig. 4B, right) and lower percentage correct on the 3-Choice SDR task ($r(15) = 0.670$, $p = 0.0064$) (Fig. 4C, right).

4. Discussion

In the current study, we observed significant diffusion changes in many gray matter regions of the cortico-basal ganglia circuit in the HTT85Q macaque model of HD. Restricted diffusion (increases in FA, and decreases in MD, RD, AD) was observed primarily in the putamen and globus pallidus, and may be the result of the selective loss of striatopallidal fibers, increased iron deposition, astrocytosis and microgliosis (Rosas et al., 2006; Douaud et al., 2009; Sanchez-Castaneda et al., 2013; Estevez-Fraga et al., 2020). Increased diffusion (reductions in FA, and increases in MD, RD, AD) was observed primarily in cortical

regions, and may be the result of cortical thinning due to neuronal loss in deep layers, and/or mHTT-induced changes in cell permeabilities/membrane integrity (Rosas et al., 2008; Delmaire et al., 2013; Odish et al., 2018). To verify this, future post-mortem histological and molecular studies using tissue from the HTT85Q and control animals are planned.

This study demonstrates the feasibility of generating AAV-based models of HD in nonhuman primates that exhibit hallmark motor and cognitive symptoms, as well as neuropathological manifestations throughout functionally relevant circuits that correlate with symptom severity. Clinical data for HD supports intervening at early stages of disease. In this context, in addition to measuring brain atrophy which may not become apparent until later stages of disease, appropriate biomarkers capable of detecting the earliest pathological changes are needed. In the HTT85Q NHP model, we have already validated several imaging markers of disease progression that are commonly used as outcome measures in clinical trials (e.g. striatal atrophy via T1-and T2-weighted MRI, alterations in white matter microstructure via DTI) (Weiss et al., 2022). Recent positron emission tomography (PET) studies in this same cohort of animals revealed signatures of ongoing cortico-basal ganglia neurodegenerative processes, including reduced glucose utilization (F18-Fluorodeoxyglucose PET) and reduced D2/D3 receptor binding (F18-Fallypride PET) (Weiss et al., 2023). Here, we continue to expand on the available set of biomarkers in this model by establishing that characteristics of gray matter diffusion are also altered early on and progress in severity over time. These results provide further validation for the use of gray matter DTI in this large animal model of HD, and will provide a new outcome measure for use in future therapeutic assessments in this model.

Funding sources

NIH/NINDS NS099136, NIH/NINDS F32NS110149, NIH/NIA T32AG055378, NIH P51OD011092 and The Bev Hartig Huntington's Disease Foundation.

CRediT authorship contribution statement

Alison R. Weiss: Conceptualization, Data curation, Formal analysis, Investigation, Methodology, Software, Supervision, Visualization, Writing – original draft, Writing – review & editing. **William A. Liguore:** Data curation, Writing – review & editing. **Kristin Brandon:** Data curation, Writing – review & editing. **Xiaojie Wang:** Data curation, Formal analysis, Investigation, Methodology, Writing – review & editing. **Zheng Liu:** Data curation, Writing – review & editing. **Christopher D. Kroenke:** Conceptualization, Investigation, Methodology, Resources, Software, Supervision, Writing – review & editing. **Jodi L. McBride:** Conceptualization, Funding acquisition, Project administration, Resources, Supervision, Writing – review & editing.

Declaration of competing interest

The authors declare the following financial interests/personal relationships which may be considered as potential competing interests: Alison Weiss, Chris Kroenke, Jodi Mcbride reports financial support was provided by National Institutes of Health. Jodi McBride reports financial support provided by The Bev Hartig Huntington's Disease Foundation.

Data availability

Data will be made available on request.

Acknowledgements

The ONPRC division of Animal Resources and Research Support was instrumental in the success of this study. We extend our sincere gratitude to the expert veterinary care and technical expertise of Lauren Drew Martin, Theodore Hobbs, Melissa Berg, Brandy Dozier, Rob Zweig, Michael Reusz, Alona Kvitky, Kristy Ritchie, Amy Kujaczynski and Isabel Bernstein.

Appendix A. Peer Review Overview and Supplementary data A Peer Review Overview

Supplementary data to this article can be found online at https://doi.org/10.1016/j.crneur.2023.100090.

References

Allen, K.L., Waldvogel, H.J., Glass, M., Faull, R.L., 2009. Cannabinoid (CB(1)), GABA(A) and GABA(B) receptor subunit changes in the globus pallidus in Huntington's disease. J. Chem. Neuroanat. 37, 266–281.

Antonsen, B.T., Jiang, Y., Veraart, J., Qu, H., Nguyen, H.P., Sijbers, J., von Horsten, S., Johnson, G.A., Leergaard, T.B., 2013. Altered diffusion tensor imaging measurements in aged transgenic Huntington disease rats. Brain Struct. Funct. 218, 767–778.

Bachevalier, J., Mishkin, M., 1986. Visual recognition impairment follows ventromedial but not dorsolateral prefrontal lesions in monkeys. Behav. Brain Res. 20, 249–261.

Chan, A.W., Jiang, J., Chen, Y., Li, C., Prucha, M.S., Hu, Y., Chi, T., Moran, S., Rahim, T., Li, S., Li, X., Zola, S.M., Testa, C.M., Mao, H., Villalba, R., Smith, Y., Zhang, X., Bachevalier, J., 2015. Progressive cognitive deficit, motor impairment and striatal pathology in a transgenic Huntington disease monkey model from infancy to adulthood. PLoS One 10, e0122335.

Delmaire, C., Dumas, E.M., Sharman, M.A., van den Bogaard, S.J., Valabregue, R., Jauffret, C., Justo, D., Reilmann, R., Stout, J.C., Craufurd, D., Tabrizi, S.J., Roos, R. A., Durr, A., Lehericy, S., 2013. The structural correlates of functional deficits in early huntington's disease. Hum. Brain Mapp. 34, 2141–2153.

Douaud, G., Behrens, T.E., Poupon, C., Cointepas, Y., Jbabdi, S., Gaura, V., Golestani, N., Krystkowiak, P., Verny, C., Damier, P., Bachoud-Levi, A.C., Hantraye, P., Remy, P., 2009. In vivo evidence for the selective subcortical degeneration in Huntington's disease. Neuroimage 46, 958–966.

Estevez-Fraga, C., Scahill, R., Rees, G., Tabrizi, S.J., Gregory, S., 2020. Diffusion imaging in Huntington's disease: comprehensive review. J. Neurol. Neurosurg. Psychiatry.

Gatto, R.G., Weissmann, C., 2019. Diffusion tensor imaging in preclinical and human studies of huntington's disease: what have we learned so far? Curr. Med. Imag. Rev. 15, 521–542.

Georgiou-Karistianis, N., Gray, M.A., Dominguez, D.J., Dymowski, A.R., Bohanna, I., Johnston, L.A., Churchyard, A., Chua, P., Stout, J.C., Egan, G.F., 2013. Automated differentiation of pre-diagnosis Huntington's disease from healthy control individuals based on quadratic discriminant analysis of the basal ganglia: the IMAGE-HD study. Neurobiol. Dis. 51, 82–92.

Glass, M., Faull, R.L., Dragunow, M., 1993. Loss of cannabinoid receptors in the substantia nigra in Huntington's disease. Neuroscience 56, 523–527.

Glass, M., Dragunow, M., Faull, R.L., 2000. The pattern of neurodegeneration in Huntington's disease: a comparative study of cannabinoid, dopamine, adenosine and GABA(A) receptor alterations in the human basal ganglia in Huntington's disease. Neuroscience 97, 505–519.

Guide for the Care and Use of Laboratory Animals, 2011. In: The National Academies Collection: Reports Funded by National Institutes of Health. Washington (DC).

Guillaume B, Hua X, Thompson PM, Waldorp L, Nichols TE, Alzheimer's Disease Neuroimaging I (2014) Fast and accurate modelling of longitudinal and repeated measures neuroimaging data. Neuroimage 94:287-302.

Huntington Study Group, 1996. Unified huntington's disease rating scale: reliability and consistency. Huntington study group. Mov. Disord. 11, 136–142.

Huntington's Disease Collaborative Research Group, 1993. A novel gene containing a trinucleotide repeat that is expanded and unstable on Huntington's disease chromosomes. Cell 72, 971–983.

Majid, D.S., Aron, A.R., Thompson, W., Sheldon, S., Hamza, S., Stoffers, D., Holland, D., Goldstein, J., Corey-Bloom, J., Dale, A.M., 2011. Basal ganglia atrophy in prodromal Huntington's disease is detectable over one year using automated segmentation. Mov. Disord. 26, 2544–2551.

McBride, J.L., Pitzer, M.R., Boudreau, R.L., Dufour, B., Hobbs, T., Ojeda, S.R., Davidson, B.L., 2011. Preclinical safety of RNAi-mediated HTT suppression in the rhesus macaque as a potential therapy for Huntington's disease. Mol. Ther. 19, 2152–2162.

O'Connell, A.B., Kuchel, T.R., Perumal, S.R., Sherwood, V., Neumann, D., Finnie, J.W., Hemsley, K.M., Morton, A.J., 2020. Longitudinal magnetic resonance spectroscopy and diffusion tensor imaging in sheep (Ovis aries) with quinolinic acid lesions of the striatum: time-dependent recovery of N-acetylaspartate and fractional anisotropy. J. Neuropathol. Exp. Neurol. 79, 1084–1092.

Odish, O.F.F., Reijntjes, R., van den Bogaard, S.J.A., Roos, R.A.C., Leemans, A., 2018. Progressive microstructural changes of the occipital cortex in Huntington's disease. Brain Imaging Behav. 12, 1786–1794.

Petrella, L.I., Castelhano, J.M., Ribeiro, M., Sereno, J.V., Goncalves, S.I., Laco, M.N., Hayden, M.R., Rego, A.C., Castelo-Branco, M., 2018. A whole brain longitudinal study in the YAC128 mouse model of Huntington's disease shows distinct trajectories of neurochemical, structural connectivity and volumetric changes. Hum. Mol. Genet. 27, 2125–2137.

Rosas, H.D., Tuch, D.S., Hevelone, N.D., Zaleta, A.K., Vangel, M., Hersch, S.M., Salat, D. H., 2006. Diffusion tensor imaging in presymptomatic and early Huntington's disease: selective white matter pathology and its relationship to clinical measures. Mov. Disord. 21, 1317–1325.

Rosas, H.D., Salat, D.H., Lee, S.Y., Zaleta, A.K., Pappu, V., Fischl, B., Greve, D., Hevelone, N., Hersch, S.M., 2008. Cerebral cortex and the clinical expression of Huntington's disease: complexity and heterogeneity. Brain 131, 1057–1068.

Sanchez-Castaneda, C., Cherubini, A., Elifani, F., Peran, P., Orobello, S., Capelli, G., Sabatini, U., Squitieri, F., 2013. Seeking Huntington disease biomarkers by multimodal, cross-sectional basal ganglia imaging. Hum. Brain Mapp. 34, 1625–1635.

Simmons, D.A., Mills, B.D., Butler Iii, R.R., Kuan, J., McHugh, T.L.M., Akers, C., Zhou, J., Syriani, W., Grouban, M., Zeineh, M., Longo, F.M., 2021. Neuroimaging, urinary, and plasma biomarkers of treatment Response in huntington's disease: preclinical evidence with the p75(NTR) ligand LM11A-31. Neurotherapeutics 18, 1039–1063.

Sprengelmeyer, R., Orth, M., Muller, H.P., Wolf, R.C., Gron, G., Depping, M.S., Kassubek, J., Justo, D., Rees, E.M., Haider, S., Cole, J.H., Hobbs, N.Z., Roos, R.A., Durr, A., Tabrizi, S.J., Sussmuth, S.D., Landwehrmeyer, G.B., 2014. The neuroanatomy of subthreshold depressive symptoms in Huntington's disease: a combined diffusion tensor imaging (DTI) and voxel-based morphometry (VBM) study. Psychol. Med. 44, 1867–1878.

Sritharan, A., Egan, G.F., Johnston, L., Horne, M., Bradshaw, J.L., Bohanna, I., Asadi, H., Cunnington, R., Churchyard, A.J., Chua, P., Farrow, M., Georgiou-Karistianis, N., 2010. A longitudinal diffusion tensor imaging study in symptomatic Huntington's disease. J. Neurol. Neurosurg. Psychiatry 81, 257–262.

Tervo, D.G., Hwang, B.Y., Viswanathan, S., Gaj, T., Lavzin, M., Ritola, K.D., Lindo, S., Michael, S., Kuleshova, E., Ojala, D., Huang, C.C., Gerfen, C.R., Schiller, J., Dudman, J.T., Hantman, A.W., Looger, L.L., Schaffer, D.V., Karpova, A.Y., 2016. A designer AAV variant permits efficient retrograde access to projection neurons. Neuron 92, 372–382.

Weiss, A.R., Liguore, W.A., Domire, J.S., Button, D., McBride, J.L., 2020. Intra-striatal AAV2.retro administration leads to extensive retrograde transport in the rhesus macaque brain: implications for disease modeling and therapeutic development. Sci. Rep. 10, 6970.

Weiss, A.R., Liu, Z., Wang, X., Liguore, W.A., Kroenke, C.D., McBride, J.L., 2021. The macaque brain ONPRC18 template with combined gray and white matter labelmap for multimodal neuroimaging studies of Nonhuman Primates. Neuroimage 225, 117517.

Weiss, A.R., Bertoglio, D., Liguore, W.A., Brandon, K., Templon, J., Link, J., McBride, J. L., 2023. Reduced D(2)/D(3) receptor binding and glucose metabolism in a macaque model of huntington's disease. Mov. Disord. 38, 143–147.

Weiss, A.R., Liguore, W.A., Brandon, K., Wang, X., Liu, Z., Domire, J.S., Button, D., Kroenke, C.D., McBride, J.L., 2022. A novel rhesus macaque model of Huntington's disease recapitulates key neuropathological changes along with progressive motor and cognitive decline. bioRxiv, 2022.2002.2002.478920.

Winkler, A.M., Ridgway, G.R., Webster, M.A., Smith, S.M., Nichols, T.E., 2014. Permutation inference for the general linear model. Neuroimage 92, 381–397.

Zuccato, C., Valenza, M., Cattaneo, E., 2010. Molecular mechanisms and potential therapeutical targets in Huntington's disease. Physiol. Rev. 90, 905–981.